# A Framework of Whole Heart Extracellular Volume Fraction Estimation for Low-Dose Cardiac CT Images

Xinjian Chen, Marcelo S. Nacif, Songtao Liu, Christopher Sibley, Ronald M. Summers,
David A. Bluemke, and Jianhua Yao

*Abstract*—Cardiac CT (CCT) is widely available and has been validated for the detection of focal myocardial scar using a delayed enhancement technique in this paper. CCT, however, has not been previously evaluated for quantification of diffuse myocardial fibrosis. In our investigation, we sought to evaluate the potential of low-dose CCT for the measurement of myocardial whole heart extracellular volume (ECV) fraction. ECV is altered under conditions of increased myocardial fibrosis. A framework consisting of three main steps was proposed for CCT whole heart ECV estimation. First, a shape-constrained graph cut (GC) method was proposed for myocardium and blood pool segmentation on postcontrast image. Second, the symmetric demons deformable registration method was applied to register precontrast to postcontrast images. So the correspondences between the voxels from precontrast to postcontrast images were established. Finally, the whole heart ECV value was computed. The proposed method was tested on 20 clinical low-dose CCT datasets with precontrast and postcontrast images. The preliminary results demonstrated the feasibility and efficiency of the proposed method.

*Index Terms*—Cardiac CT (CCT), extracellular volume (ECV) fraction, myocardium segmentation, registration.

## I. INTRODUCTION

DIFFUSE myocardial fibrosis is an increasingly recognized pathologic endpoint that is observed in association with a variety of cardiomyopathies and heart failure. Myocardium extracellular volume (ECV) fraction is increased in association with diffuse myocardial fibrosis, a hallmark of pathologic remodeling [1]. Cardiac magnetic resonance imaging (CMRI) has been well validated and allows quantification of myocardial fibrosis in comparison to overall mass of the myocardium [2]. CMRI T1 mapping with ECV determination [3], [4] is a novel method to quantify diffuse fibrosis noninvasively, and has been

X. Chen is with the School of Electrical and Information Engineering, Soochow University, Jiangsu 215006, China (e-mail: xjchen@suda.edu.cn).

M. S. Nacif, S. Liu, C. Sibley, R. M. Summers, D. A. Bluemke, and J. Yao are with the Department of Radiology and Imaging Sciences, National Institute of Health, Bethesda, MD 20892 USA (e-mail: marcelo.nacif@mail.nih.gov; songtao.liu@mail.nih.gov; christopher.sibley@mail.nih.gov; rsummers@mail.nih.gov; bluemked@mail.nih.gov; jyao@mail.nih.gov).

Corresponding author, Jianhua Yao, phone: 301-402-3225; fax: 301-496-9933.
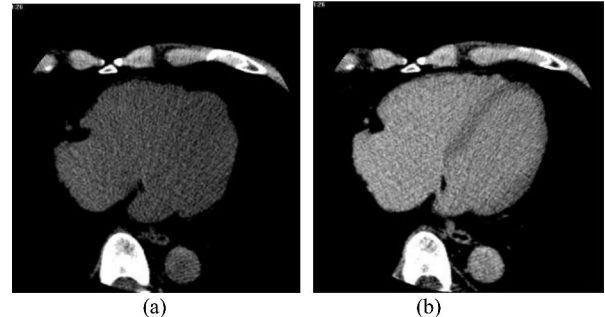
Fig. 1. Examples of two phases of CCT: (a) precontrast; (b) postcontrast.

validated under multiple conditions, including myocardial infarction, heart failure, aortic regurgitation, and cardiomyopathy. Unfortunately, CMRI is relatively expensive, time consuming, and contraindicated in patients with intracardiac devices and irregular heart beat. In addition, claustrophobia is present in about 5% or more of CMRI subjects [5]. Cardiac CT (CCT) has emerged as a common and widespread technology and also has been validated for the detection of focal myocardial scar [6] and myocardial stress/rest perfusion [7]. CCT acquisition is much faster but is less sensitive to contrast differences than CMRI. In this paper, we sought to evaluate the potential of low-dose CCT for the measurement of myocardial 3-D whole heart ECV fraction.

There are several investigations related to ECV fraction computation [3]–[5], [8]. In all of these methods, the ECV fraction was computed based on multiple 2-D regions of interest (ROI). However, the diffuse fibrosis is a global process and a whole heart ECV estimation is highly desirable for clinical application. In order to compute the 3-D ECV fraction, pixel-to-pixel correspondence between the precontrast and postcontrast images needs to be established. This can be accomplished by registration methods. Fig. 1 shows examples of precontrast and postcontrast CCT images. As we can see from the figure, it is nearly impossible to differentiate myocardium and blood pool in the precontrast image and the segmentation of myocardium and blood pool in the postcontrast image which is also a challenging task. For accurate 3-D ECV fraction computation, advanced registration and segmentation methods are highly desired. A brief review of the related segmentation and registration methods is given below.

The segmentation of the cardiac images has been the motivation of many research works. The cardiac image segmentation

methods [9] may be classified into several types: image-based [9]–[15], model-based [16]–[22], and hybrid methods [23]–[26]. Image-based methods perform segmentation based on the image information available in the image; these include edge detection [10], [11], active contours [12], [13], level set (LS) [14], fuzzy connectedness [15], and graph cut (GC) [16]. These methods perform well on high-quality images. However, the results are not as good when the image quality is inferior or boundary information is missing. In recent years, there has been an increasing interest in model-based segmentation methods. One advantage of these methods is that, even when some boundary information is missing, such gaps can be filled due to the introduced prior knowledge present in the model. These models were based on different geometric and physical representations, including spring–mass models [17], triangle-based finite-element models [18], simplex meshes [19], finite-element models [20], 3-D B-spline deformation fields [21], and statistical shape and appearance models [22]–[24]. The hybrid approaches are rightfully attracting a great deal of attention at present. The synergy that exists between these two approaches—image-based and model-based strategies—is clearly emerging in the segmentation field. As such, hybrid methods that form a combination of two or more approaches are emerging as powerful segmentation tools where their superior performances and robustness over each of the components are beginning to be well demonstrated [25]–[28]. In this paper, the cardiac segmentation is based on an advanced hybrid method which effectively integrates the GC method with the shape information computed from the live wire (LW) method [29]. There are several shape prior-integrated segmentation methods that have been proposed, such as shape prior-integrated LS methods [30], [31] and shape prior-integrated GC methods [27], [28]. The LS method has been widely used; however, it is computationally demanding and requires a decent initialization so as to not fall into a local minimum. We propose to apply the shape-integrated GC method to take advantage that the GC method can compute the global optimum solution for the two-label segmentation and enforce piecewise smoothness [16]. The shape-integrated GC methods further improve the GC by effectively combining the shape prior information. In this paper, the shape prior information is computed via the LW method [29], which is a user-steered 2-D segmentation method and performs optimal delineation based on dynamic programming.

Image registration is not a trivial task and cardiac image registration is a more complex problem in particular because of the nonrigid and mixed motions of the heart and the thorax structures. Moreover, as compared to other organ's registration such as brain, the heart exhibits fewer accurate anatomical landmarks. Also, cardiac images are usually acquired with a lower resolution than brain images. The commonly used cardiac registration methods could be classified into two main categories: those based on geometric image features [27]–[29] and those based on voxel similarity measures [30]–[38]. The geometric image feature-based methods are divided into registration of a set of points [32] and edges or surfaces [33], [34]. Registration methods based on voxel similarity measures include moments and principal-axes methods [35], [36], intensity difference and correlation methods [37], [38], atlas-based method [39] and

methods based on mutual information [40], [41]. The demons algorithm [42] is a well-established technique for nonrigid registration. One of the most efficient methods is the demons algorithm proposed by Thirion [43]. Several variants of the algorithm have been proposed depending on how the forces are computed, such as ad hoc symmetrization of the demons force [44] and symmetric forces [45]. Vercauteren *et al.* [46] explained from a theoretical point of view that the symmetric forces demons algorithm is more efficient in practice. In this paper, the symmetric demons deformable registration method is applied for the registration due to its efficiency.

In this paper, we propose a novel framework for 3-D whole heart ECV fraction estimation on low-dose CCT images. The proposed framework consists of three main steps. First, a hybrid segmentation method is proposed for myocardium and blood pool segmentation on postcontrast image. The hybrid method contains two steps: initialization and segmentation. A pseudo-3-D strategy is applied for the initialization based on LW method. Then the shape information generated from the initialization step is integrated into the GC cost function, and this shape prior-integrated GC is applied for the finer segmentation. Second, a symmetric demons deformable registration method is applied to register precontrast to postcontrast images. So the correspondences between the voxels from precontrast to postcontrast images were established. Finally, the whole heart ECV value was computed. Our contributions in this paper are summarized as follows.

To the best of our knowledge, we are the first to propose a framework of 3-D whole heart ECV estimation using low-dose CCT Images.

For the myocardium and blood pool segmentation, we propose an advanced segmentation method that integrates the shape prior information generated from the LW method with that generated with the GC method. For the registration of precontrast and postcontrast images, we apply the symmetric demons method.

The rest of this paper is organized as follows. In Section II, we elaborate the complete methodology of the 3-D whole heart ECV fraction computation. In Section III, we evaluate the performance of the proposed method. In Section IV, we provide discussions and conclusions.

## II. METHOD AND MATERIALS

### A. Overview of the Approach

A flowchart of the proposed method is shown in Fig. 2. The proposed framework consists of three main steps: shape-constrained GC-based segmentation, symmetric demons-based registration, and ECV computation. Among these three steps, the segmentation and registration are the core parts of the proposed framework. The details are given in each section next.

### B. Myocardium and Blood Pool Segmentation Based on a Shape-Constrained GC Method

The proposed segmentation method consists of two main steps. First, the cardiac contour is initialized to generate the
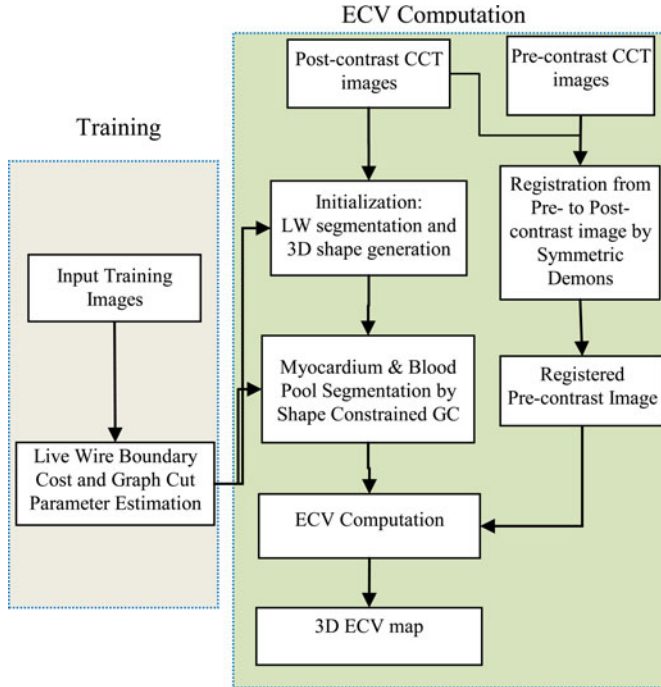
Fig. 2.    Flowchart of the proposed method.

rough object shape information. Second, the shape information is integrated into the GC cost computation, and then the shape-constrained GC is used for the myocardium and blood pool segmentation.

*1) Initialization:* The objective of the initialization is to generate the shape constraints for the latter GC segmentation. The initialization consists of two steps: first, the cardiac contour is initialized by segmenting the top, middle, and bottom slices via the LW method, and then the contours in between are linearly interpolated so that the 3-D shape contour is generated. The LW segmentation is conducted on only three slices due to two reasons: 1) The LW is a user-steered 2-D segmentation method, i.e., it needs user input for the landmarks and is time consuming. 2) Three slices are sufficient to generate the rough shape, which will be refined by the latter GC segmentation. During the process of LW segmentation, the user provides the landmarks on the boundary; then the LW method will do the delineation automatically [29]. The user usually only needs to provide about ten landmarks per slice.

An oriented boundary cost function is devised for myocardium contour as per the LW method [29]. Following the original terminology and notation in [29], we define a boundary element, *bel* for short, as an oriented edge between two pixels. For a given image slice $I$, a *bel* will be represented as an ordered pair $(p, q)$ of four adjacent pixels where $p$ is inside the object (pixel value 1) and $q$ is outside (pixel value 0). We think of every pixel edge of $I$ as constituting two potential *bels* $(p, q)$ and $(q, p)$ and possibly assign different cost values to them. To every *bel* of $I$, we assign a set of features depending on the orientation $(p, q)$ or $(q, p)$. The features assigned to each *bel* are intended to express the likelihood of the *bel* belonging to the boundary of a particular object of interest. In our particular case, the cost

$c(l)$ associated with *bel l* is a linear combination of the costs assigned to its features

$$c(l) = \frac{\sum_{i=1}^{nf} w_i c_f(f_i(l))}{\sum_{i=1}^{nf} w_i} \qquad (1)$$

where nf is the number of features, $w_i$ is a positive constant indicating the emphasis given to feature $f_i$, and $c_f$ is the function to convert feature values $f_i(l)$ at l to cost values $c_f(f_i(l))$. In LW [29], $f_i$ may represent features such as intensity on the immediate interior of the boundary, intensity on the immediate exterior of the boundary, and gradient magnitude at the center of the *bel*. Depending on the intensity characteristics of the object of interest, different $f_i$ may be combined. As suggested in [29], $c_f$ is chosen as an inverted Gaussian function, and all selected features are combined with weights $w_i$. We utilize the feature of LW to define the best-oriented path between any two landmark points ($x_k$ and $x_{k+1}$) as a sequence of *bels* with minimum total cost:

$$K(x_k, x_{k+1}) = \sum_{i=1}^{h} c(l_i) \qquad (2)$$

where $h$ represents the number of *bels* in the best-oriented path $\langle l_1, l_2, \ldots, l_h \rangle$. The total cost structure $K(\mathbf{x})$ associated with all the landmarks may now be defined as

$$K(\mathbf{x}) = \sum_{k=1}^{m} \kappa(x_k, x_{k+1}) \qquad (3)$$

where $m$ is the number of landmarks for the object of interest and we assume that $x_{m+1} = x_1$ (closed contour). In other words, $K(\mathbf{x})$ is the sum of the costs associated with the best oriented paths between all $m$ pairs of successive landmarks of shape instance $\mathbf{x}$. The parameters of $K(\mathbf{x})$ for each object shape $\mathbf{x}$ are estimated automatically as described in [29] by using the training images.

*2) Shape-Constrained GC Method:* We propose a shape-constrained GC method for the myocardium and blood pool segmentation. The proposed algorithm effectively integrates the shape information from an initialization step with the optimal 3-D delineation capability of the GC method.

GC segmentation can be formulated as an energy minimization problem such that for a set of pixels $P$ and a set of labels $L$, the goal is to find a labeling $f: P \to L$ that minimizes the energy function $\text{En}(f)$:

$$\text{En}(f) = \sum_{p \in P} R_p(f_p) + \sum_{p \in P, \, q \in N_p} B_{p,q}(f_p, f_q) \qquad (4)$$

where $N_p$ is the set of pixels in the neighborhood of $p$, $R_p(f_p)$ is the cost of assigning label $f_p \in L$ to $p$, and $B_{p,q}(f_p, f_q)$ is the cost of assigning labels $f_p, f_q \in L$ to $p$ and $q$. In two-class labeling, $L = \{0, 1\}$, the problem can be solved efficiently with GCs in polynomial time when $B_{p,q}$ is a submodular function, i.e., $B_{p,q}(0, 0) + B_{p,q}(1, 1) \le B_{p,q}(0, 1) + B_{p,q}(1, 0)$ [47].

In our framework, the unary cost $R_p(f_p)$ is the sum of a data penalty $D_p(f_p)$ and a shape penalty $S_p(f_p)$ term. The data term is defined based on image intensity and can be considered as a log likelihood of the image intensity for the target object. The

shape prior term is independent of image information, and the boundary term is based on the gradient of the image intensity.

The proposed shape-integrated energy function is defined as follows:

$$\text{En}(f) = \sum_{p \in P} \left( \alpha \cdot D_p(f_p) + \beta \cdot S_p(f_p) \right)$$
$$+ \sum_{p \in P, \, q \in N_p} \gamma \cdot B_{p,q}(f_p, f_q) \quad (5)$$

where $\alpha, \beta, \gamma$ are the weights for the data term $S_p$, shape term $S_p$, and boundary term, respectively, satisfying $\alpha + \beta + \gamma = 1$. These components are defined as follows:

$$D_p(f_p) = \begin{cases} -\ln P(I_p|O), & \text{if } f_p = \text{object label} \\ -\ln P(I_p|B), & \text{if } f_p = \text{background label} \end{cases} \quad (6)$$

$$B_{p,q}(f_p, f_q) = \exp\left( -\frac{(I_p - I_q)^2}{2\sigma^2} \right) \cdot \frac{1}{d(p,q)} \cdot \delta(f_p, f_q) \quad (7)$$

and

$$\delta(f_p, f_q) = \begin{cases} 1, & \text{if } f_p \neq f_q \\ 0, & \text{otherwise} \end{cases} \quad (8)$$

where $I_p$ is the intensity of pixel $p$; object label is the label of the object (foreground); $P(I_p|O)$ and $P(I_p|B)$ are the probability of intensity of pixel $p$ belonging to object and background, respectively, which are estimated from object and background intensity histograms during the training phase (details given below); $d(p,q)$ is the Euclidian distance between pixels $p$ and $q$; and $\sigma$ is the standard deviation of the intensity differences of neighboring voxels along the boundary

$$S_p(f_p) = 1 - \exp\left( -\frac{d(p, \mathbf{x}_O)}{r_O} \right) \quad (9)$$

where $d(p, \mathbf{x}_O)$ is the distance from pixel $p$ to the set of pixels which constitute the interior of the current shape $\mathbf{x}_o$ of object $O$ (note that if $p$ is in the interior of $\mathbf{x}_o$, then $d(p, \mathbf{x}_O) = 0$); $r_O$ is the radius of a circle that just encloses $\mathbf{x}_o$. During the implementation for the data term $D$, if the probability is 0, then a very small value (such as $10\text{e}-10$) will be assigned instead, so this value will not go up to infinity. And a normalization step is also performed to make the value to be within [0, 1]. The linear time method of [48] was used in this paper for computing this distance.

*3) Minimizing En With GCs:* The minimization of (5) can be solved by the GC method. The graph is designed as follows. We take $V = P \cup L$, i.e., $V$ contains all the pixel nodes and terminals corresponding to the labels in $L$ which represent objects of interest plus the background. $A = A_N \cup A_T$, where $A_N$ is the *n*-links which connect pixels $p$ and $q$ ($p \in P, q \in N_p$) and with a weight of $w_p, q$. $A_T$ is the set of *t*-links which connect pixel $p$ and terminals $\ell \in L$ and with a weight of $w_{p,\ell}$. The desired graph with cut cost $|C|$ equaling $\text{En}(f)$ is constructed using the following weight assignments:

$$w_{p,q} = \gamma \cdot B_{p,q} \quad (10)$$
$$w_{p,l} = M - (\alpha \cdot D_p(\ell) + \beta \cdot S_p(\ell)) \quad (11)$$

where $M$ is constant that is large enough to make the weights $w_{p,\ell}$ positive.

## C. Deformable Registration by Symmetric Demons Algorithm

In order to compute the 3-D ECV fraction, the pixel-to-pixel correspondence between the precontrast and postcontrast images must be established. In this paper, the symmetric deformable demons registration method is applied. The demons algorithm has been widely used for images registration field and achieved good results. The demons method is a nonparametric nonrigid image registration method. It alternates between computation of the optical flow forces and regularization by a Gaussian smoothing.

The demons algorithm could be seen as an optimization of a global energy. The main idea is to introduce a hidden variable in the registration process: correspondences. We then consider the regularization criterion as a prior on the smoothness of the transformation. Instead of requiring that point correspondences between image pixels be exact realizations of the transformation, one allows some error at each image point. For the symmetric forces demons registration, the modification was made to avoid large deformations when gradients have small values [46]. Vercauteren *et al.* [46] explained from a theoretical point of view that the symmetric forces demons algorithm is more efficient in practice, which is the main reason to choose this technique in our system. We use the implementation contributed by Corinne Mattmann, ETH Zurich, Switzerland. The registration program was implemented using components of the open-source segmentation and registration toolkits [49], which are cross-platform C++ software toolkits and are freely available from http://www.itk.org.

The influence of the standard deviation $\sigma$ of the Gaussian kernel used during the demons registration process to the deformation field is studied. This parameter is related to the regularity of the estimated deformation field: the higher the $\sigma$, the smoother the deformation field. And the influence of the number of iterations on the convergence of the algorithm and on the CPU time is also studied.

## D. ECV Fraction Computation

After registration, the correspondences of the voxels between the precontrast and postcontrast images were established. Myocardial and blood pool Hounsfield unit attenuation values at each voxel were recorded and ECV fraction was computed as follows:

$$\text{ECV} = (\Delta\text{HU}_{\text{myocardium}}/\Delta\text{HU}_{\text{blood}}) * (1 - \text{Hct}_{\text{blood}}) \quad (12)$$

where Hct is the hematocrit and $\Delta\text{HU}$ is the change in Hounsfield unit attenuation ($\Delta\text{HU} = \text{HU}_{\text{post iodine}} - \text{HU}_{\text{pre iodine}}$).

## III. EXPERIMENTAL RESULTS

The proposed methods were tested on a clinical CCT dataset. This dataset contained images of 20 subjects [ten heart failure subjects with ten age- and gender-matched controls, ages

60.9 $\pm$ 7.2 (mean $\pm$ st.dev.)], acquired from the precontrast and postcontrast phases of a 320-MDCT scanner (Aquilion One, Toshiba Medical Systems, Tustin, CA). The slice thickness is 3 mm and the in-plane pixel size is $0.37 * 0.37$ mm. The image size is $512 * 512 * 47$.

## A. Parameters Training

In this paper, the leave-one-out strategy is used for the evaluation. The parameters of LW and shape-integrated GC methods are optimized through the training. We have ten postcontrasted CCT images, i.e., when testing on one image, other nine images will be used for training. The parameters of the LW method, such as number of features and weight for each feature, are optimized through the training. For more details, see [29], and the executable version can be downloaded from http://www.mipg.upenn.edu/cavass/. The parameters of the GC method are determined also through the training stage. The intensity histograms for each object are estimated from the training images. Based on this, $P(I_p|O)$ and $P(I_p|B)$ can be computed. As for parameters $\alpha, \beta,$ and $\gamma$ in (5), since $\alpha + \beta + \gamma = 1$, we estimate only $\alpha$ and $\beta$ by optimizing accuracy as a function of $\alpha$ and $\beta$ and set $\gamma = 1 - \alpha - \beta$. We use the gradient descent method for the optimization. Let $\text{Accu}(\alpha, \beta)$ represent the algorithm's accuracy (here we use the true positive volume fraction [50]); $\alpha$ and $\beta$ are initialized to 0.35 each, and then $\text{Accu}(\alpha, \beta)$ is optimized over the training dataset to determine the best $\alpha$ and $\beta$.

## B. Evaluation of the Segmentation Method

An expert in CCT imaging field manually segmented the postcontrast cardiac images and the results were used as the references for the segmentation evaluation. Fig. 3 shows the myocardium and blood pool segmentation results on three slices. From visual checking, we can find that the results are quite good.

The quantitative evaluation of the proposed approach results is presented in Table I. The accuracy in terms of true-positive and false-positive volume fractions (TPVF and FPVF) [51], and average surface distance are shown. TPVF indicates the fraction of the total amount of tissue in the true delineation; FPVF denotes the amount of tissue falsely identified, which are defined as follows:

$$\text{TVPF} = \frac{|C_{\text{TP}}|}{|C_{\text{td}}|} \tag{13}$$

$$\text{FPVF} = \frac{|C_{\text{FP}}|}{|U_d - C_{\text{td}}|}. \tag{14}$$

where $U_d$ is assumed to be a binary scene with all voxels in the scene domain set to have a value 1, $C_{td}$ is the set of voxels in the true delineation, and $|\cdot|$ denotes volume. More details can be seen in [50].

## C. Evaluation of Registration

Fig. 4 shows the comparison of registration results by affine registration and the proposed method on three slices. We can see from it that before registration the overlap is not good due
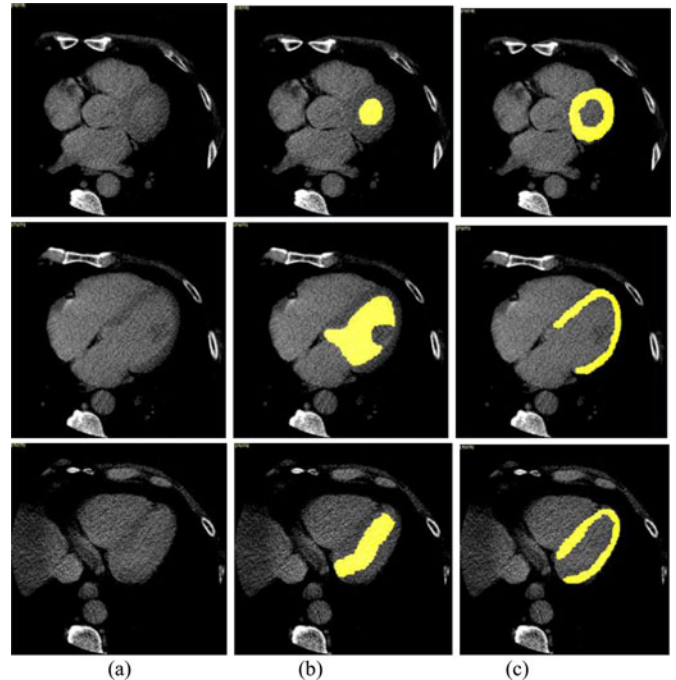


Fig. 3. Myocardium and blood pool segmentation results by the proposed shape-constrained GC method on one patient's postcontrast-enhanced image—three slices. (a) Original image. (b) Blood pool segmentation result. (c) Myocardium segmentation result.

TABLE I
MEAN AND STANDARD DEVIATION OF TPVF, FPVF, AND AVERAGE SURFACE DISTANCE FOR THE PROPOSED METHOD ON POSTCONTRAST IMAGE

| | TPVF (%) | FPVF (%) | Average Surface Dist (mm) |
|---|---|---|---|
| Myocardium | 92.2 ±1.5 | 0.66 ±0.12 | 0.72 ±0.39 |
| Blood Pool | 93.2 ±1.1 | 0.52 ±0.09 | 0.66 ±0.31 |

to the large deformations, while after registration by the proposed method two images overlap perfectly. Compared to affine registration, the proposed symmetric forces demons registration method achieved much better results.

The alignment of ROIs is a good indicator of how well two images are registered [51]. In this paper, the average relative overlap accuracy (AROA) is used for the quantitative evaluation of the registration method. The relative overlap of segmentations is a measure of how well two corresponding segmented regions agree with each other. Twenty ROIs have been selected by an imaging expert according to the following criteria: 1) wide distribution of ROIs throughout the CCT image and 2) simple and accurate identification of all the ROIs. Fig. 5 shows some examples of selected ROIs. The AROA is computed based on all the ROIs as follows:

$$\text{AROA} = \frac{1}{N} \sum_{i=1}^{N} \frac{\text{ROI}_x(i) \cap \text{ROI}_y(i)}{\text{ROI}_x(i) \cup \text{ROI}_y(i)} \tag{15}$$

where $\text{ROI}_x(i)$ and $\text{ROI}_y(i)$ being the $i$th corresponding ROI in the two images, and $N$ is the number of ROIs.
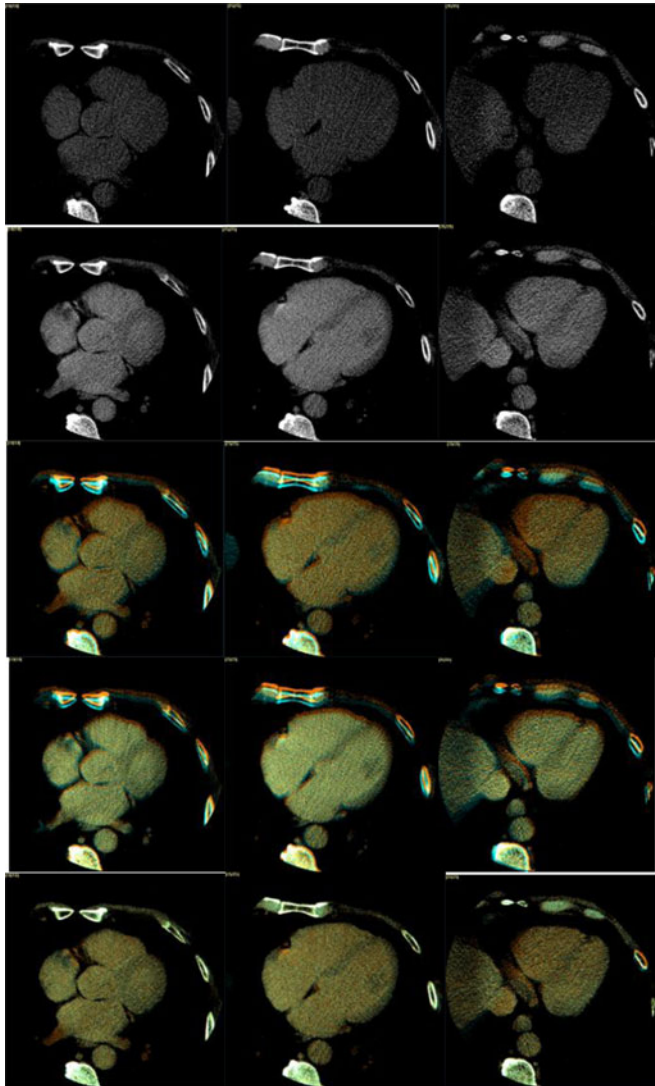
| Σ | 0.5 | 1 | 2 | 3 | 4 | 5 |
|---|---|---|---|---|---|---|
| *AROA (%)* | 84.6 | 89.2 | 89.6 | 90.3 | 90.2 | 90.1 |

| Number of iterations | *AROA* (%) | CPU time (min.) |
|---|---|---|
| 10 | 84.1 | 2.2 |
| 20 | 87.9 | 3.8 |
| 50 | 90.3 | 10.0 |
| 80 | 90.4 | 14.5 |
| 100 | 90.5 | 18.2 |

Table III shows the influence of the number of iterations on the landmark mapping and on the CPU time. As expected, the CPU time increases linearly with the number of iterations. Beyond 50 iterations, the improvement in the accuracy is no longer significant. This value was adopted for the experiments presented in this paper.

In terms of efficiency, the average computation time for the initialization, segmentation, and registration on an Intel Xeon E5440 workstation with 2.83 GHz CPU, 8 GB of RAM was 1, 1, and 10 min, respectively. The time for the ECV map computation is very little, so it is neglected. The whole process is fast and acceptable for the clinical use.

### D. Reproducibility Analysis of the Proposed Method

The proposed method consists of two steps, initialization and segmentation, in which the segmentation is fully automatic; however, initialization step needs user interaction. So the reproducibility analysis was performed for the proposed method. User1 (XC) performed the proposed method (3-D whole heart) twice and User2 (MN) performed the proposed method (3-D whole heart) once. The same reproducibility analysis was performed to the manual method and the results were compared to the proposed method. Fig. 6 shows the linear regression analysis results of the proposed method versus manual on mean myocardium density. We can see from that the proposed 3-D whole heart ECV method has much higher reproducibility ($R^2$ is 0.963 and 0.961 for intra and inter, respectively) than the manual method ($R^2$ is 0.917 and 0900 for intra and inter, respectively).

### E. Statistical Correlation Analysis Between Manual and Proposed Methods

In clinical settings, ECV is typically measured using several 2-D ROIs. CCT data were first reformatted to the short-axis plane to correspond to the CMRI acquisition, then myocardial and blood pool attenuation values at the base, mid, and apex were measured twice, and the average value was used for analysis. Here, the statistical correlation analysis between



Fig. 4. Symmetric demons registration results on one patient's three slices. The first row shows the precontrast image; the second shows the postcontrast image; the third row shows the overlap of the precontrast (cyan color) over the postcontrast image (orange color); the fourth row shows the overlap of the registered precontrast (cyan color) by affine registration over the postcontrast image (orange color); and the last row shows the overlap of registered precontrast (cyan color) by the symmetric forces demons over the postcontrast image (orange color).
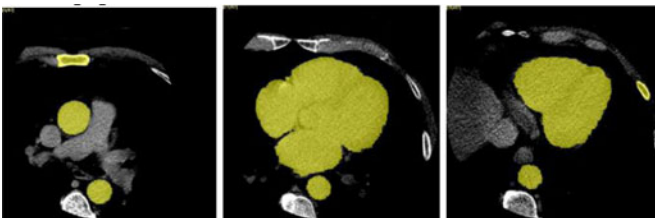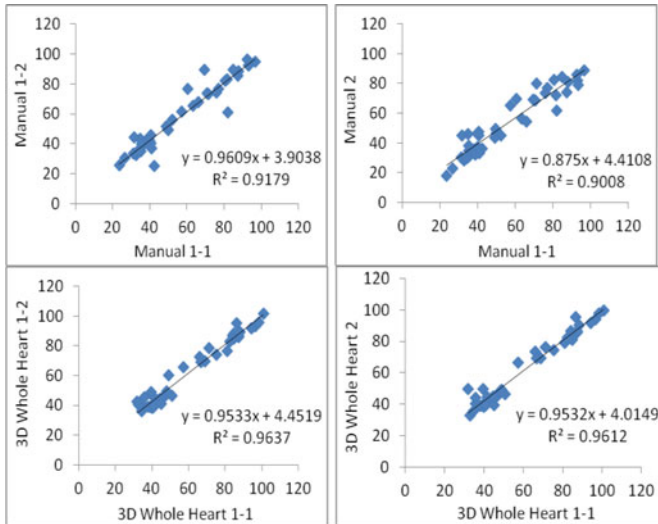


Fig. 5. Examples of selected ROIs.

Table II shows the influence of the standard deviation $\sigma$ of the Gaussian kernel used during the demons registration process to the deformation field. Results showed that the best performance was reached for $\sigma = 3$ and this value was adopted in this paper.
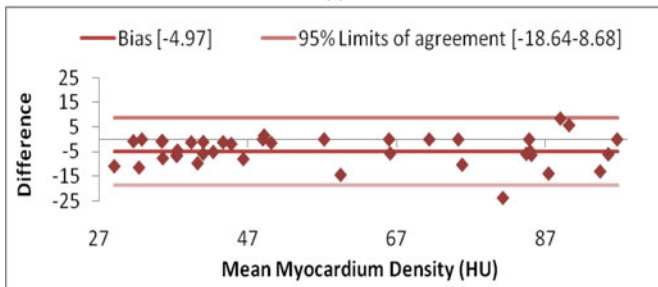
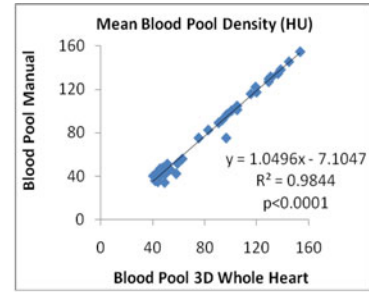Fig. 6. Reproducibility analysis results of the proposed method versus manual on mean myocardium density (HU).
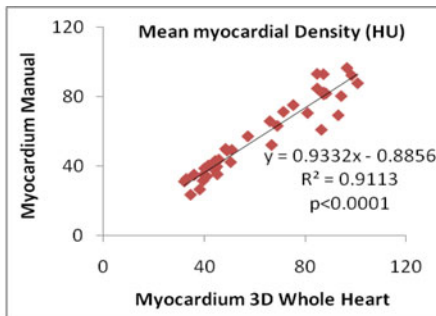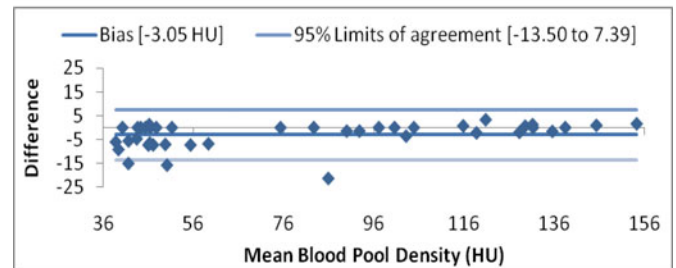


Fig. 7. Results of mean myocardium density obtained by the manual and proposed methods (3-D whole heart). (a) Linear regression analysis and (b) Bland–Altman analysis.



Fig. 8. Results of mean blood pool density obtained by the manual and proposed methods (3-D whole heart). (a) Linear regression analysis and (b) Bland–Altman analysis.
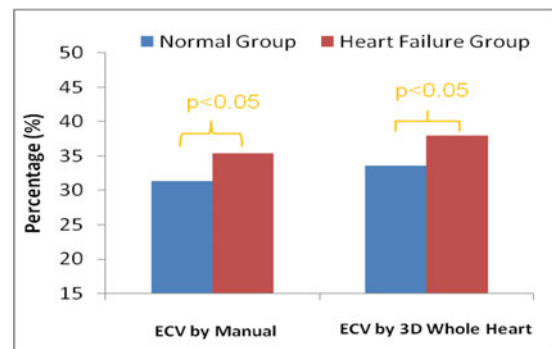


Fig. 9. Differentiation between normal and heart failure groups using ECV by the manual and proposed methods (3-D whole heart).

the proposed and manual methods was performed. The linear regression analysis and Pearson's correlation were used to examine the relationship between automated and manual results. The Bland–Altman method was also used to calculate the bias and limits of agreement. $P$-values $<0.05$ were considered to be statistically significant.

Figs. 7 and 8 show the linear regression and Bland–Altman analysis results of mean myocardium and blood pool density obtained by manual and proposed methods, respectively. We can see that the proposed method achieved high correlation with the manual results on myocardium and blood pool density. As the ECV value is computed based on the myocardium and blood pool intensity, it is natural to find that they are highly correlated. Fig. 9 shows the differentiation between normal and heart failure groups using ECV value by manual and proposed methods (3-D whole heart). We can see from that similar to the manual analysis, the proposed method can differentiate the normal and heart failure groups. It is worthy to note that the proposed method gives higher overall percentage than the manual method. This is due to the registration that the proposed method gets better contrast between pre- and postdata; therefore the ECV value is higher, which better reflects the real value than the manual method. Fig. 10 shows the visualization results of 3-D ECV map on normal and heart failure subjects. We can find that the heart failure subject has much higher ECV values for most voxels than normal subject.

## IV. CONCLUSIONS AND DISCUSSIONS

In this paper, we proposed a framework for the 3-D whole heart ECV estimation for low-dose CCT images. The proposed
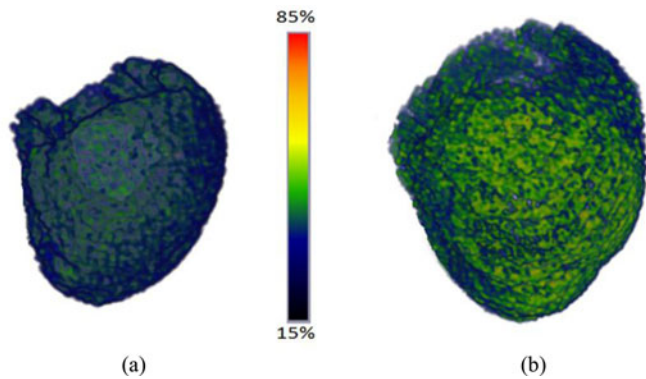
Fig. 10. Visualization of 3-D CCT ECV map on two subjects. (a) Normal subject. (b) Heart failure subject. The heart failure subject has much higher ECV values for most voxels than a normal subject.
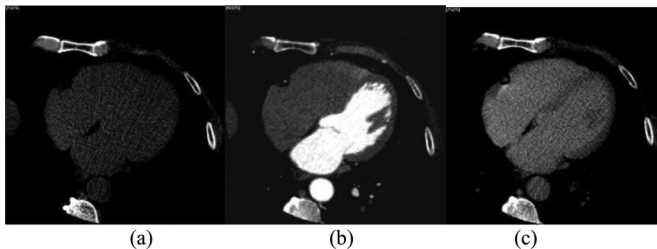


Fig. 11. Three-phase CCT images. (a) Precontrast image; (b) CT angiography image; (c) postcontrast Image.

framework consists of three main steps: 1) myocardium and blood pool segmentation based on a shape-constrained GC method; 2) pre- and postcontrast cardiac images registration based on symmetric demons algorithm; and 3) ECV value computation. The proposed method was tested on 20 clinical low-dose CCT datasets with precontrast and postcontrast images. The preliminary results show that 1) the good segmentation and registration performance demonstrated the feasibility and efficiency of the proposed method. 2) The proposed method achieved high correlations with manual analysis results. 3) The proposed method has much higher reproducibility than the manual method.

Here, we investigated a semiautomatic 3-D ECV estimation method based on two CCT phases: precontrast and postcontrast. Compared to the three-phase (as shown in Fig. 11) method, two CCT scans result in less radiation exposure for the patient. And another issue is CT angiography image generally acquired at different phase compared with CCT pre- and postcontrast images. However, when the CT angiography scan is used, the blood pool can be easily segmented by the threshold method (see Fig. 11(b)) and then this blood pool can be used as a shape constraint for myocardium segmentation based on the shape-constrained GC method, which makes the whole framework fully automatic. The fully automatic framework will be investigated in the near future.

In the clinical environment, CMRI has been validated for the detection of myocardial fibrosis, in which ECV fraction was used as an important factor. However, for CMRI, the ECV fraction was usually computed based on several 2-D ROIs. In this paper, we computed the 3-D whole heart ECV fraction based on the low-dose CCT images. The statistical analysis was performed between the proposed method and manual ECV analysis results. We find from the results that the proposed method achieved high correlation with the manual results. However, the proposed method was tested on only 20 CCT images. The proposed method will be tested on more dataset in the near future.

REFERENCES

[1] E. B. Schelbert, S. M. Testa, C. G. Meier, W. J. Ceyrolles, J. E. Levenson, A. J. Blair, P. Kellman, B. L. Jones, D. R. Ludwig, D. Schwartzman, S. G. Shroff, and T. C. Wong, "Myocardial extravascular extracellular volume fraction measurement by gadolinium cardiovascular magnetic resonance in humans: Slow infusion versus bolus," *J. Cardiovasc. Magn. Reson.*, pp.13:16, Mar. 4, 2011.

[2] A. S. Flett, M. P. Hayward, M. T. Ashworth, M. S. Hansen, A. M. Taylor, P. M. Elliott, C. McGregor, and J. C. Moon, "Equilibrium contrast cardiovascular magnetic resonance for the measurement of diffuse myocardial fibrosis: Preliminary validation in humans," *Circulation*, vol. 122, pp. 138–144, 2010.

[3] W. G. Hundley, D. A. Bluemke, J. P. Finn, S. D. Flamm, M. A. Fogel, M. G. Friedrich, V. B. Ho, M. Jerosch-Herold, C. M. Kramer, W. J. Manning, M. Patel, G. M. Pohost, A. E. Stillman, R. D. White, and P. K. Woodard, "ACCF/ACR/AHA/NASCI/SCMR 2010 expert consensus document on cardiovascular magnetic resonance: A report of the American college of cardiology foundation task force on expert consensus documents," *Circulation*, vol. 121, no. 22, pp. 2462–2508, 2010.

[4] C. Sibley, J. Huang, M. Ugander, A. Oki, J. Han, M. S. Nacif, A. Greiser, D. R. Messroghli, P. Kellman, A. E. Arai, D. A. Bluemke, and S. Liu, "Myocardial and blood T1 quantification in normal volunteers at 3T," *J. Cardiovasc. Magn. Reson.*, vol. 13, pp. 51, 2011.

[5] P. Sparrow, D. R. Messroghli, S. Reid, J. P. Ridgway, G. Bainbridge, and M. U. Sivananthan, "Myocardial T1 mapping for detection of left ventricular myocardial fibrosis in chronic aortic regurgitation: Pilot study," *Amer. J. Roentgenol.*, vol. 187, pp. W630–W635, 2006.

[6] S. R. Heckbert, W. Post, G. D. Pearson, D. K. Arnett, A. S. Gomes, M. Jerosch-Herold, W. G. Hundley, J. A. Lima, and D. A. Bluemke, "Traditional cardiovascular risk factors in relation to left ventricular mass, volume, and systolic function by cardiac magnetic resonance imaging: The Multiethnic study of atherosclerosis," *J. Amer. Coll. Cardiol.*, vol. 48, pp. 2285–2292, 2006.

[7] T. Senra, A. A. Shiozaki, V. M. Salemi, and C. E. Rochitte, "Delayed enhancement by multidetector computed tomography in endomyocardial fibrosis," *Eur. Heart J.*, vol. 329, p. 347, 2008.

[8] O. Craciunescu, D. Brizel, E. Cleland, D. Yoo, N. Muradyan, M. Carroll, D. Barboriak, and J. MacFall, "Dynamic contrast enhanced-MRI in head and neck cancer patients: Variability of the precontrast longitudinal relaxation time (T10)," *Med. Phys.*, vol. 37, no. 6, pp. 2683–2692, 2010.

[9] C. Petitjean and J.-N. Dacher, "A review of segmentation methods in short-axis cardiac images," *Med. Image Anal.*, vol. 15, pp. 169–184, 2011.

[10] J. Canny, "A computational approach to edge detection," *IEEE Trans. Pattern Anal. Mach. Intell.*, vol. 8, no. 6, pp. 769–798, Jun. 1986.

[11] R. Deriche, "Using Canny's criteria to derive a recursively implemented optimal edge detector," *Int. J. Comput. Vision*, vol. 1, pp. 167–187, 1987.

[12] A. Singh, L. Kurowski, and M. Chiu, "Cardiac MR image segmentation using deformable models," in *Proc. SPIE—Int. Soc. Opt. Eng.*, 1993, vol. 1905, no. 8, pp. 8–28.

[13] M. Kass, A. Witkin, and D. Terzopoulos, "Snakes: Active contour models," *Int. J. Comput. Vision*, vol. 1, pp. 321–332, 1988.

[14] A. Charnoz, D. Lingrand, and J. Montagnat, "A levelset based method for segmenting the heart in 3D+T gated SPECT image," in *Proc. Int. Workshop Functional Imag. Modeling Heart*, 2003, p. 2674.

[15] J. K. Udupa and S. Samarasekera, "Fuzzy connectedness and object definition: Theory, algorithms, and applications in image segmentation," *Graph. Models Image Process.*, vol. 58, no. 3, pp. 246–261, 1996.

[16] Y. Boykov and V. Kolmogorov, "An experimental comparison of min-cut/max-flow algorithms," *IEEE Trans. Pattern Anal. Mach. Intell.*, vol. 26, no. 9, pp. 1124–1137, Sep. 2004.

[17] C. Nastar and N. Ayache, "Frequency-based nonrigid motion analysis: Application to four dimensional medical images," *IEEE Trans. Pattern Anal. Mach. Intell.*, vol. 18, no. 11, pp. 1067–1079, Nov. 1996.

[18] J. Park, D. Metaxas, and L. Axel, "Analysis of left ventricular motion based on volumetric deformable models and MRISPAMM," *Med. Image Anal.*, vol. 1, no. 1, pp. 53–71, 1996.

[19] O. Gerard, A. Collet-Billon, J.-M. Rouet, M. Jacob, M. Fradkin, and C. Allouche, "Efficient model-based quantification of left ventricle function in 3D echocardiography," *IEEE Trans. Med. Imag*, vol. 21, no. 9, pp. 1059–1068, Sep. 2002.

[20] M. Sermesant, Y. Coudiere, H. Delingette, and N. Ayache, "Progress towards an electro-mechanical model of the heart for cardiac image analysis," in *Proc. IEEE Int. Symp. Biomed. Imag.*, 2002, pp. 10–13.

[21] R. Chandrashekara, A. Rao, G. I. Sanchez-Ortiz, R. H. Mohiaddin, and D. Rueckert, "Construction of a statistical model for cardiac motion analysis using non-rigid image registration," in *Proc. 18th Int. Conf. Inf. Process. Med. Imag.*, 2003, vol. 2732, pp. 599–610.

[22] A. F. Frangi, D. Rueckert, J. A. Schnabel, and W. J. Niessen, "Automatic construction of multiple object three-dimensional statistical shape models: Application to cardiac modeling," *IEEE Trans. Med. Imag.*, vol. 21, no. 9, pp. 1151–1166, Sep. 2002.

[23] M. Üzümcü, A. F. Frangi, M. Sonka, J. H. C. Reiber, and B. P. F. Lelieveldt, "ICA vs. PCA active appearance models: Application to cardiac MR segmentation," in *Proc. Med. Image Comput. Comput.-Assist. Interven.*, 2001, pp. 451–458.

[24] Y. Zheng, A. Barbu, B. Georgescu, M. Scheuering, and D. Comaniciu, "Four-chamber heart modeling and automatic segmentation for 3D cardiac CT volumes using marginal space learning and steerable features," *IEEE Trans. Med. Imag.*, vol. 27, no. 11, pp. 1668–1681, Nov. 2008.

[25] X. Lin, B. Cowan, and A. Young, "Model-based graph cut method for segmentation of the left ventricle," in *Proc. 27th Annu. Int. Conf. Eng. Med. Biol. Soc.*, 2005, vol. 3, pp. 3059–3062.

[26] J. Suri, "Segmentation and quantification techniques for fitting computer vision models to cardiac MR, CT, C-ray and PET image data," in *Advanced Algorithmic Approaches to Medical Image Segmentation*, J. Suri, S. Setarehdan, and S. Singh, Eds.: Springer-Verlag, London Limited, 2002, pp. 131–227.

[27] J. J. Malcolm, Y. Y. Rathi, and A. A. Tannenbaum, "Graph cut segmentation with nonlinear shape priors," in *Proc. IEEE Int. Conf. Image Process.*, 2007, vol. IV, pp. 365–368.

[28] N. Vu and B. S. Manjunath, "Shape prior segmentation of multiple objects with graph cuts," in *Proc. IEEE Comput. Soc. Conf. Comput. Vision Pattern Recog.*, 2008, pp. 1–8.

[29] A. X. Falcao, J. K. Udupa, S. Samarasekera, and S. Sharma, "User-steered image segmentation paradigms: Live wire and live lane," *Graph. Models Image Process.*, vol. 60, pp. 233–260, 1998.

[30] D. Cremers, S. J. Osher, and S. Soatto, "Kernel density estimation and intrinsic alignment for shape priors in level set segmentation," *Int. J. Comput. Vision*, vol. 69, no. 3, pp. 335–351, 2006.

[31] T. Chan and W. Zhu, 2003. Level set based shape prior segmentation, Tech. Rep. 03-66. Los Angeles: Computational Applied Mathematics, UCLA.

[32] M. A. Wirth, C. Choi, and A. Jennings, "Point-to-point registration of nonrigid medical images using local elastic transformation methods," in *Proc. IEEE Int. Conf. Image Process. Its Appl.*, Jul. 1997, vol. 2, pp. 780–784.

[33] T. H. Mäkelä, P. Clarysse, J. Lötjönen, O. Sipilä, K. Lauerma, H. Hänninen, E.-P. Pyökkimies, J. Nenonen, J. Knuuti, T. Katila, and I. E. Magnin, "A new method for the registration of cardiac PET and MR images using deformable model based segmentation of the main thorax structures," in *Medical Image Computing and Computer Assisted Intervention* (Lecture Notes in Computer Science, 2208), Springer-Verlag, Berlin, Heidelberg, 2001, pp. 557–564.

[34] M. A. Audette, F. P. Ferrie, and T. M. Peters, "An algorithmic overview of surface registration techniques for medical imaging," *Med. Image Anal.*, vol. 4, pp. 201–217, 2000.

[35] D. Dey, P. J. Slomka, L. J. Hahn, and R. Kloiber, "Automatic three dimensional multimodality registration using radionuclide transmission CT attenuation maps: A phantom study," *J. Nucl. Med.*, vol. 40, no. 3, pp. 448–455, 1999.

[36] R. Wan and M. Li, "An overview of medical image registration," in *Proc. 5th Int. Conf. Comput. Intell. Multimedia Appl.*, 2003, pp. 385–390.

[37] G. J. Klein, N. W. Reutter, and R. H. Huesman, "Four-dimensional affine registration models for respiratory-gated PET," *IEEE Trans. Nucl. Sci.*, vol. 48, no. 3, pp. 756–760, Jun. 2001.

[38] N. S. Phatak, S. A. Maas, A. I. Veress, N. A. Pack, E. V. Di Bella, and J. A. Weiss, "Strain measurement in the left ventricle during systole with deformable image registration," *Med. Image Anal.*, vol. 13, no. 2, pp. 354–361, 2009.

[39] B. C. Vemuri, J. Ye, Y. Chen, and C. M. Leonard, "Image registration via level-set motion: Applications to atlas based segmentation," *Med. Image Anal.*, vol. 7, pp. 1–20, 2003.

[40] W. M. Wells, P. Viola, H. Atsumi, S. Nakajima, and R. Kikinis, "Multimodal volume registration by maximization of mutual information," *Med. Image Anal.*, vol. 1, no. 1, pp. 35–51, 1996.

[41] P. W. Josien, J. B. Pluim, Ma. Antoine, and M. A. Viergever, "Mutual information based registration of medical images: A survey," *IEEE Trans. Med. Imag.*, vol. 22, no. 8, pp. 986–1004, Aug. 2003.

[42] T. Vercauteren, X. Pennec, A. Perchant, and N. Ayache, "Diffeomorphic demons: Efficient non-parametric image registration," *NeuroImage*, vol. 45, pp. S61–S72, 2009.

[43] J. P. Thirion, "Image matching as a diffusion process: An analogy with Maxwell's demons," *Med. Image Anal.*, vol. 2, no. 3, pp. 243–260, 1998.

[44] H. Wang, L. Dong, J. O'Daniel, R. Mohan, A. S. Garden, K. K. Ang, D. A. Kuban, M. Bonnen, J. Y. Chang, and R. Cheung, "Validation of an accelerated 'demons' algorithm for deformable image registration in radiation therapy," *Phys. Med. Biol.*, vol. 50, no. 12, 2005.

[45] T. Vercauteren, X. Pennec, A. Perchant, and N. Ayache, "Symmetric log-domain diffeomorphic registration: A demons-based approach," in *Proc. 11th Int. Conf. Med. Image Comput. Comput.-Assist. Interven.*, New York, NY, Sep. 6–10, 2008, pp. 754–761.

[46] T. Vercauteren, X. Pennec, E. Malis, A. Perchant, and N. Ayache, "Insight into efficient image registration techniques and the demons algorithm," *Inf. Process. Med. Imag.*, vol. 4584/2007, pp. 495–506, 2007.

[47] V. Kolmogorov and R. Zabih, "What energy functions can be minimized via graph cuts?" *IEEE Trans. Pattern Anal. Mach. Intell.*, vol. 26, no. 2, pp. 147–159, 2004.

[48] K. C. Ciesielski, X. Chen, J. K. Udupa, and G. J. Grevera, "Linear time algorithms for exact distance transform," *J. Math. Imag. Vision*, vol. 39, no. 3, pp. 193–209, 2011.

[49] Insight Segmentation and Registration Toolkit (ITK), (2011). [Online]. Available: http://www.itk.org/

[50] J. K. Udupa, V. R. Leblanc, Y. Zhuge, C. Imielinska, H. Schmidt, L. M. Currie, B. E. Hirsch, and J. Woodburn, "A framework for evaluating image segmentation algorithms," *Comput. Med. Imag. Graph.*, vol. 30, no. 2, pp. 75–87, 2006.

[51] J. M. Fitzpatrick, D. L. G. Hill, Y. Shyr, J. West, C. Studholme, and C. R. Maurer, "Visual assessment of the accuracy of retrospective registration of MR and CT images of the brain," *IEEE Trans. Med. Imag.*, vol. 17, no. 4, pp. 571–585, Aug. 1998.

**Xinjian Chen** received the Ph.D. degree from the Center for Biometrics and Security Research, Key Laboratory of Complex Systems and Intelligence Science, Institute of Automation, Chinese Academy of Sciences, Beijing, China, in 2006.

After completing the graduation, he joined Microsoft Research Asia where he was involved in research on handwriting recognition. From January 2008 to May 2012, he has conducted the Postdoctoral Research at several prestigious groups: Medical Image Processing Group, Department of Radiology, University of Pennsylvania (January 2008–October 2009); Department of Radiology and Image Sciences, Clinical Center, National Institutes of Health (October 2009–August 2011); Prof. Milan Sonka's Group, Department of Electrical and Computer Engineering, University of Iowa (September 2011–May 2012). He is currently with the School of Electrical and Information Engineering, Soochow University, Jiangsu, China, as a Full Professor. His research interests include medical image processing and analysis, pattern recognition, machine learning, and their applications.

**Marcelo S. Nacif** received the M.D. degree from the Serra dos Órgãos University, Teresópolis, Rio de Janeiro, Brazil, in 2001. His training includes a fellowship in diagnostic Radiology at the "Carlos Chagas Post-Graduation Institute" at Rio de Janeiro from 2002 to 2005 and a fellowship in Magnetic Resonance Imaging at the "Hospital de Clínicas de Niterói" from 2005 to 2006. He received the Master of Medicine degree in radiology and the Ph.D. degree from Rio de Janeiro Federal University, where he studied the use of magnetic resonance applied to advanced cardiovascular imaging, specializing in noninvasive angiography and cardiac MR from 2004 to 2009.

He is currently a Postdoctoral Visiting Fellow at the Department of Radiology and Imaging Science, Clinical Center, National Institutes of Health, Bethesda, MD. Also, he has a postdoctoral research fellowship position at the Cardiology Division, Johns Hopkins School of Medicine, Baltimore.

**Songtao Liu,** photograph and biography not available at the time of publication.

**Christopher Sibley,** photograph and biography not available at the time of publication.

**Ronald M. Summers** received the B.A. degree in physics and the M.D. and Ph.D. degrees in medicine/anatomy and cell biology from the University of Pennsylvania, Philadelphia.

He completed a medical internship at the Presbyterian-University of Pennsylvania Hospital, Philadelphia a radiology residency at the University of Michigan, Ann Arbor, and an MRI fellowship at Duke University, Durham, NC. In 1994, he joined the Diagnostic Radiology Department, NIH Clinical Center, Bethesda, MD, where he is now a tenured Senior Investigator and Staff Radiologist. He is currently the Chief of the Clinical Image Processing Service and directs the Imaging Biomarkers and Computer-Aided Diagnosis (CAD) Laboratory. He has coauthored more than 200 journal, review, and conference proceedings articles and is a coinventor of 10 patents. His research interests include virtual colonoscopy, CAD, multiorgan multiatlas registration, and development of large radiologic image databases. His clinical areas of specialty are thoracic and gastrointestinal radiology and body cross-sectional imaging.

Dr. Summers received the Presidential Early Career Award for Scientists and Engineers, presented by Dr. N. Lane, President Clinton's science advisor, in 2000. He is a member of the editorial boards of the journals *Radiology* and *Academic Radiology*. He is a program committee member of the computer-aided diagnosis program of the annual SPIE Medical Imaging conference.

**David A. Bluemke,** photograph and biography not available at the time of publication.

**Jianhua Yao** received the B.S., M.S., and Ph.D. degrees in computer science from Tianjin University, Tianjin, China; Tsinghua University, Beijing, China; and Johns Hopkins University, MD, respectively.

He joined the National Institutes of Health (NIH) in 2002 as a Staff Scientist, where he directs a clinical image processing laboratory. He is also affiliated with the Imaging Biomarker and Computer-Aided Diagnosis Laboratory, NIH. He has published more than 150 papers in journals and conference proceedings, and holds two patents in colon cancer CAD technique. His research interests include clinical image processing, deformable model, nonrigid registration, CAD, and CT colonography.